Vernier optical phased array lidar transceivers: supplement

NATHAN DOSTART,[1,2,*] ⓘ BOHAN ZHANG,[3] ⓘ MICHAEL BRAND,[1] ⓘ
KENAISH AL QUBAISI,[3] DENIZ ONURAL,[3] DANIEL FELDKHUN,[1]
MILOŠ POPOVIĆ,[3] ⓘ AND KELVIN WAGNER[1] ⓘ

[1]*Department of Electrical, Computer, and Energy Engineering, University of Colorado, Boulder, Colorado 80309, USA*
[2]*Currently with NASA Langley Research Center, Hampton, Virginia 23681, USA*
[3]*Department of Electrical and Computer Engineering, Boston University, Boston, Massachusetts 02215, USA*
[*]*nathan.a.dostart@nasa.gov*

Vernier optical phased array lidar transceivers: supplementary material

This document provides supplementary information to "Vernier optical phased array lidar transceivers." The supplementary material includes additional theoretical and numerical assessment of the Vernier transceiver concept. It discusses the performance of the Vernier concept relative to aperiodic designs, optimal lobe suppression design for arbitrary apodizations, and additional considerations for wavelength-steered phased arrays.

1. COMPARISON TO APERIODIC ARRAYS

In order to provide a direct comparison between the grating lobe suppression offered by the Vernier transceiver approach and aperiodic OPAs, we consider an example lidar system composed of a single 1D TX OPA and adjacent RX OPA, both with 32 gratings. Four cases are considered in conjunction with an example scene: a monostatic system using a periodic OPA, a monostatic system using an aperiodic OPA, a bistatic system with non-identical aperiodic OPAs, and the Vernier transceiver (bistatic, non-identical periodic OPAs). Note that the monostatic cases are also equivalent to a bistatic system using identical TX/RX OPAs when the target is in the far-field of the transceiver.

The aperiodic arrays are designed in accordance with [1], where a periodic array of waveguides is placed with a uniformly random distribution between $[3, 5]$ µm spacing to achieve the single main lobe and flat, white noise background of the grating lobes. Different random distributions are used between the TX and RX OPAs. The OPAs all have the same average pitch of 4 µm between gratings, each grating being 500 nm wide, to provide a direct comparison. We note here that an aperiodic array with a given minimum pitch will have a larger average pitch than a periodic array with the same minimum pitch. For the Vernier case, the $k = 2$ condition is used such that the RX OPA has only 30 gratings and a pitch of $4.27 = (32/30)4$ µm.

The emission patterns of the 4 OPA designs are shown in Fig. S1. The aperiodic OPAs do not exhibit strong grating lobes as in the periodic designs, at the cost of an approximately white noise distribution of lobes across the entire hemisphere. The 32 grating design and unoptimized random grating distribution of the aperiodic OPAs yields a 5-7 dB suppression of grating lobes relative to the periodic OPAs. An 'ideal' aperture, for this case a uniform rect emission pattern occupying the same area as the OPAs, is plotted for comparison. The intensity patterns for all emission patterns are normalized to the peak intensity of the ideal aperture. For all OPA designs, the main lobe experiences a -9 dB insertion loss relative to the ideal aperture due to emission into the grating lobes.

The example scene used is shown in Fig. S2(a). The target is assumed to be in the far-field of the lidar system and is composed of a constant background with low (1%) diffuse reflection and three distinct targets: 1) a 100% reflectivity delta function at $\theta = 0°$, 2) a 50% reflectivity rect at $22°$ (the grating lobe spacing), and 3) a one-sided triangle reaching up to 20% reflectivity at $-9°$. All targets are assumed to be diffuse, which is modeled by applying a random reflection phase at each spatial pixel of the target scene. The received power is calculated using Eq. 5 from the main text, normalized by the power received by the ideal aperture for the 100% reflectivity delta function. The received power is calculated for 100 different iterations of random target phases, while keeping the reflectivity constant, in order to average over the inherent intensity fluctuations due to speckle. This example looks purely at the received power as a function of scan angle, neglecting ranging operations, though received power in a lidar system should be directly proportional to the values shown here.

The received power for each system configuration is shown in Fig. S2(b). The OPA-based systems receive 18 dB less power than in the ideal aperture case, simply from paying the -9 dB insertion loss penalty twice (once on transmit, a second time on receive). The monostatic periodic OPA (or bistatic identical periodic OPAs) case shows clear evidence of grating lobe-induced spurious signals, where the rect and delta functions are repeated three times within this FOV and the triangle twice. In this case the target's reflectivity, size, and location are all ambiguous, highlighting the necessity for grating lobe suppression techniques. By contrast, both aperiodic designs and the Vernier approach all significantly suppress these spurious signals (see for example the highlighted regions, where no signal should exist). These suppression approaches also help
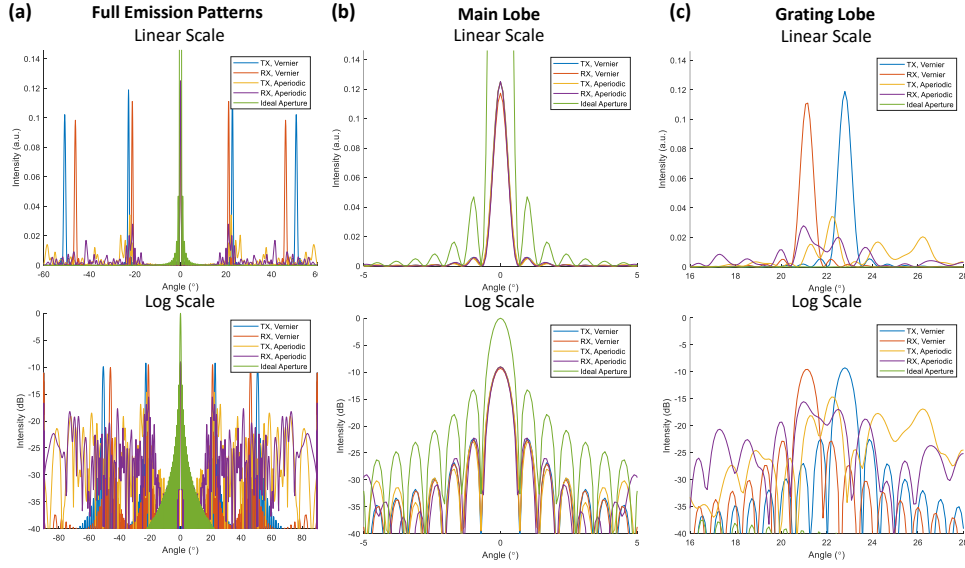
Fig. S1. Emission patterns of example arrays. (a) Emission pattern across entire hemisphere in linear (top) and log (bottom) scales. Note the random spurs arising for the aperiodic array. (b) Main lobe. Note the more rapid fall-off of sidelobes for the aperiodic OPAs. (c) Grating lobe. The aperiodic design suppresses the grating lobe by approximately 5 dB, and the different aperiodic designs have different (randomized) lobe locations.

mitigate the effects of the low background reflectivity, improving SNR and target detection – for the monostatic periodic OPA, the signals are only ~ 10 dB above the background. Using a grating lobe suppression approach, the signal level is essentially unchanged but the background is reduced by 5–8 dB. We note that the bistatic aperiodic case, which to our knowledge has not been explored in the literature, shows somewhat improved performance over the monostatic aperiodic case. It can be seen that for all steering angles the $k = 2$ Vernier case provides superior performance with lower background and reduced spurious signal without compromising on the actual signal level. This advantage, a 1–2 dB reduction in background and spurious grating lobe signals over the bistatic aperiodic approach, will likely be reduced with larger grating count OPAs as the aperiodic designs are better able to avoid accidental 'lobes' as the grating count increases.

2. CHOICE OF OPTIMAL RX ARRAY

While in the body of the paper we restricted the RX array to have few gratings and larger pitch than the TX array, and heuristically arrived at the condition to align the first grating lobe TX peak with an RX null, we show here that these conditions can be arrived at by considering the maximum grating lobe suppression. For a set of beams emitted by the TX array, and an equivalent set of beams comprising the detection pattern of the RX array, we can evaluate the overlap integral equivalent to the (power) detection efficiency of the mth TX beam with the nth RX beam in transverse spatial frequency space as

$$\eta_{m,n} = \left| \int_{-\infty}^{\infty} df_x F_{TX}^m(f_x) F_{RX}^n(f_x) \right|^2 \tag{S1}$$

where $F(f_x)$ denotes the field emission/reception pattern as a function of the transverse spatial frequency, as in the main text. For periodically spaced emitters, the beams will also be spaced periodically in the transverse spatial frequency domain. If the periods of the TX and RX arrays are close, and considering beams near broadside, then the mth TX beam will only overlap significantly with the mth RX beam, such that we can assume all $\eta_{m,n} = 0$ for $n \neq m$. In order to suppress grating lobes we desire $\eta_{m,m} = 0$ for $m \neq 0$, requiring the overlap integral in Eq. Eq. (S1) to evaluate to null.

Considering the same TX and RX apertures as in the main text, the offset $\Delta f_x(m)$ between the mth beam pair centers is determined by their respective grating pitches for broadside emission as
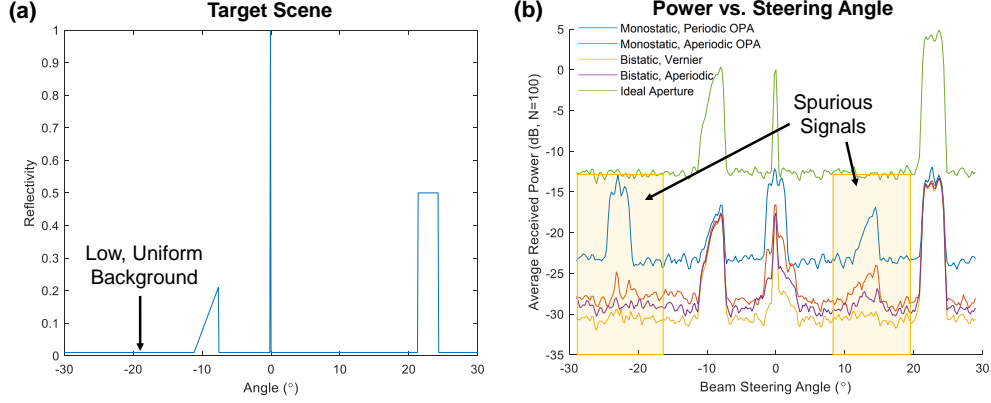
Fig. S2. Target scene and reconstructed image for each approach. (a) Far-field target scene, including 3 distinct targets as well as a low, constant background reflectivity (1%). (b) Received power as a function of beam-steering angle for all cases. The power is normalized to that received by the ideal aperture for the 100% reflectivity delta function at broadside. Note the spurious signals arising due to grating lobes highlighted in gold, as well as the non-zero background which varies between implementations.

$$\Delta f_x(m) = m \left(\frac{1}{\Lambda_{TX}} - \frac{1}{\Lambda_{RX}} \right) \tag{S2}$$

and the overlap integral for the mth beam pair can therefore be written in angular space as

$$\int_{-\infty}^{\infty} df_x \text{sinc}\left(W_{TX}(f_x - \Delta f_x(m))\right) \text{sinc}\left(W_{RX}f_x\right) = 0 \tag{S3}$$

where we have suppressed the amplitude scaling factors, set the RX beam to be centered at $f_x = 0$, and identified the aperture widths as $W_i = N_i \Lambda_i$.

By choosing to set this integral to 0, rather than minimize the overlap function $F_{RX}F_{TX}$, we have chosen to suppress grating lobes for the case of large targets – when all the transmitted power intercepts the target and is reflected back – rather than point targets. In the large target case, the signal is proportional to total power in the beam, so we desire to maximize the power received from the main lobe and minimize the power received from other lobes (minimize the overlap integral). For unresolved (point) targets, the signal is proportional to beam intensity rather than power and in that case we would minimize the received intensity from other lobes (minimize the overlap function).

Noting that this integral can be evaluated as a convolution of the form

$$\left[\text{sinc}\left(W_{TX}f_x\right) * \text{sinc}\left(W_{RX}f_x\right)\right]_{\Delta f_x(m)} = 0 \tag{S4}$$

we Fourier transform the convolution to get a multiplication of rects, the two aperture functions. We therefore have

$$\left[\mathcal{F}^{-1}\left\{\text{rect}\left(\frac{x}{W_{TX}}\right)\text{rect}\left(\frac{x}{W_{RX}}\right)\right\}\right]_{\Delta f_x(m)} = 0. \tag{S5}$$

However, this can be easily simplified to a single rect with the width of the *smaller* aperture. Therefore, for a given TX array width, there is no effect on the overlap (grating lobe suppression) by making the RX array *larger* than the TX array. However, if the RX array is smaller than the TX array the overlap will be affected (negatively, as we will show). This will motivate choosing an RX array the same size as the TX array.

Denoting the effective aperture width as $W = \min[W_{TX}, W_{RX}]$, the null overlap condition is

$$\text{sinc}\left(W\Delta f_x(m)\right) = 0. \tag{S6}$$

This condition sets a restriction on the beam center offset Δf_x which can be understood more intuitively as choosing to align the peak of one radiation pattern with the null of the other. Specifically, we require for $m \neq 0$ (i.e. all grating lobes, but excluding the overlapping main lobes)

$$W\Delta f_x(m) = n, \quad n \in \mathbb{Z} : n \neq 0 \tag{S7}$$

or equivalently

$$W\left(\frac{1}{\Lambda_{TX}} - \frac{1}{\Lambda_{RX}}\right) = n, \quad n \in \mathbb{Z} : n \neq 0. \tag{S8}$$

Notably, for $N_{TX} - N_{RX} = k$, and choosing identically sized TX and RX arrays $W = W_{TX} = W_{RX}$ (thereby setting $\Lambda_{RX} = \Lambda_{TX}N_{TX}/N_{RX}$), this null overlap is guaranteed. This can be seen by evaluating the null overlap condition which is

$$W\left(\frac{1}{\Lambda_{TX}} - \frac{1}{\Lambda_{RX}}\right) = k \tag{S9}$$

recovering the solution we arrived at in the body of the paper heuristically.

We note here that smaller aperture widths, which determine the effective overlap width W, increase the minimum pitch difference between the TX and RX arrays required to reach a given null of the sinc. Other considerations, in particular power loss to unused grating lobes, motivate small pitches for *both* the TX and RX arrays. One therefore desires to use the smallest pitch possible for both arrays, and for one array the pitch is sacrificed in order to achieve this peak-null alignment for grating lobe suppression. One should then avoid worsening this sacrifice by decreasing the RX array width below the TX array width, and there is no benefit gained with regard to grating lobes suppression by making the RX array larger than the TX array. This consideration therefore motivates making both arrays the same size, again arriving at a conclusion which was intuitively arrived at the in the main body of the paper.

3. GRATING LOBE NULLING WITH ARBITRARY APODIZATION

Regarding other apodization patterns, in general this method of 'perfect' grating lobe suppression using the Vernier method can be applied to any apodization function with few restrictions. For the purposes of the derivation we will restrict both TX and RX arrays to have the same apodization, but the same method is applicable for any combination of apodizations so long as the correlation of their Fourier transforms has a zero-crossing.

For identical TX and RX array apodizations, to achieve ideal grating lobe suppression we require an apodization which, when squared, has a Fourier transform with at least one zero-crossing. More specifically, we require that the aperture amplitude (without restrictions on phase) be a function $f(x)$ such that $\mathcal{F}^{-1}\{f^2(x)\} = 0$ for some spatial frequency $f_x = a$. In order to suppress *all* grating lobes simultaneously, the nulls of the Fourier transform should be periodic and aligned to $f_x = 0$. Notably, the vast majority of windowing/apodization functions meet these criteria [2], with a few exceptions such as the Hanning-Poisson window [3]. Any window function which is not 'smooth', or continuous at all derivatives throughout the window, will have positive and negative sidelobes in the Fourier domain interspersed with periodic zeroes [3]. The set of functions which are smooth and have compact support are classified by mathematicians as 'mollifiers' [4]. However, this smoothness is a necessary but not sufficient criterion to avoid sidelobes; some functions within this set will still have sidelobes, such as the 'standard' mollifier [5].

Taking the null overlap condition for a general far-field distribution $F(f_x) = \mathcal{F}\{f(x)\}$ we have

$$\int_{-\infty}^{\infty} df_x F(f_x) F(f_x - \Delta f_x) = 0. \tag{S10}$$

Noting again that this equation is identical to an auto-convolution, we can rewrite the equation as

$$[F(f_x) * F(f_x)]_{\Delta f_x} = 0 \tag{S11}$$

or, in the Fourier domain,

$$\left[\mathcal{F}^{-1}\left\{f^2(x)\right\}\right]_{\Delta f_x} = 0. \tag{S12}$$

The suppression condition is easily obtained by choosing Δf_x as the location of a null of the auto-correlation of $F(f_x)$. For different apodizations, we equivalently require

$$[F(f_x) \star G(f_x)]_{\Delta f_x} = 0. \tag{S13}$$

4

If this condition is enforced for the first grating lobe pair, the null periodicity about the symmetry plane ensures that all higher order grating lobes are also suppressed.

4. DESIGN CONSIDERATIONS FOR STEERING MODES IN SOPAS

The SOPA design presents a unique consideration for Vernier beam steering, as the emitters no longer have fully independent delay lines – the emitter length factors into the incremental delay. Using the temporal delay interpretation of steering, we can write the phase step for the SOPA design as

$$
\begin{aligned}
\Delta\phi(\Delta\omega) &= \tau\Delta\omega \\
&= \Delta\omega\left(\tau_g + \tau_f + 2\tau_{\text{bend}}\right)
\end{aligned}
\tag{S14}
$$

where τ_g is the delay in the grating (emitter), τ_f is the delay in the flyback waveguide, and τ_{bend} is the delay in one taper-bend-taper structure, so that $\tau_g + \tau_f + 2\tau_{\text{bend}}$ is one full row-to-row delay. Here τ_{bend} incorporates the delay of a single adiabatic $180°$ bend and the two tapers required to connect the grating waveguide to the flyback waveguide.

For simplicity we consider only changing τ_f and τ_g as the bend and taper designs are significantly constrained by the desire to minimize loss over the operating bandwidth. We additionally assume τ_{bend} is identical in both TX and RX OPAs (i.e. unaffected by the difference in row-to-row pitches Λ_{TX}, Λ_{RX}). In practice, the bend delay will vary slightly between the two OPAs which modifies the optimal design. While one could control the delay by engineering the group index, the waveguide lengths are much simpler to define and, unlike the group index, unaffected by fabrication variations in layer thickness or composition. For a given grating cross-section and a (different) flyback cross-section there will be two group indices n_g^g (grating), n_g^f (flyback) which we assume are identical for TX and RX SOPAs.

Under the restriction of equal flyback and grating lengths L_g, the row-to-row delay is

$$
\tau = 2\tau_{\text{bend}} + \frac{L_g}{c}\left(n_g^g + n_g^f\right)
\tag{S15}
$$

allowing us to set the grating length according to the steering mode. As stated previously in Eqs. 10a/b in the main text, the tracking and sliding modes respectively correspond to

$$
\tau_{RX} = \frac{\Lambda_{RX}}{\Lambda_{TX}}\tau_{TX}
\tag{S16}
$$

$$
\tau_{RX} = \tau_{TX}.
\tag{S17}
$$

While the sliding mode implies that both TX and RX SOPAs should have identical grating lengths, the tracking mode requires $\tau_{RX} > \tau_{TX}$ for $\Lambda_{RX} > \Lambda_{TX}$ with $N_{RX} + k = N_{TX}$. In this case one needs longer grating and flyback waveguides to achieve the increased delay. An intuitive solution is found in the case where the delay in the bends can be neglected, in which case $L_g^{RX} = \Lambda_{RX}/\Lambda_{TX}L_g^{TX}$. Recalling our suggested configuration of $N_{TX}\Lambda_{TX} = N_{RX}\Lambda_{RX}$ for Vernier nulling of grating lobes, it can be seen that the same phase delay condition enforces that the total waveguide length of the transmit and receive arrays be identical $N_{TX}L_g^{TX} = N_{RX}L_g^{RX}$ when there is no delay in the bends. This would be the starting condition for a real design incorporating tapers and bends in which the receive waveguide length L_g^{RX} would be varied to give $\tau_{RX} = \tau_{TX}$ across the beamsteering bandwidth.

5. COMPARISON OF STEERING MODES

It is worth making a few comments at this point on both Vernier steering modes which, upon further examination, will point to an optimized steering mode which outperforms either of these basic approaches. Several different FOVs will be referenced in this section, which we clarify here. The element function provides a fundamental limit on the FOV which could be achieved by any OPA design, and for an emitter with width w the element FOV in the spatial frequency domain is $\text{FOV}_e = 2\pi/d$. The grating lobe-limited FOV, which any periodic OPA will be limited to if a Vernier transceiver design is not used, is $\text{FOV}_g = 2\pi/\Lambda$ where Λ denotes the pitch of the emitters. Finally, for a Vernier transceiver design, there is an FOV over which two lobes remain aligned and power can be emitted/received. This FOV can be considered as the effective FOV of the Vernier
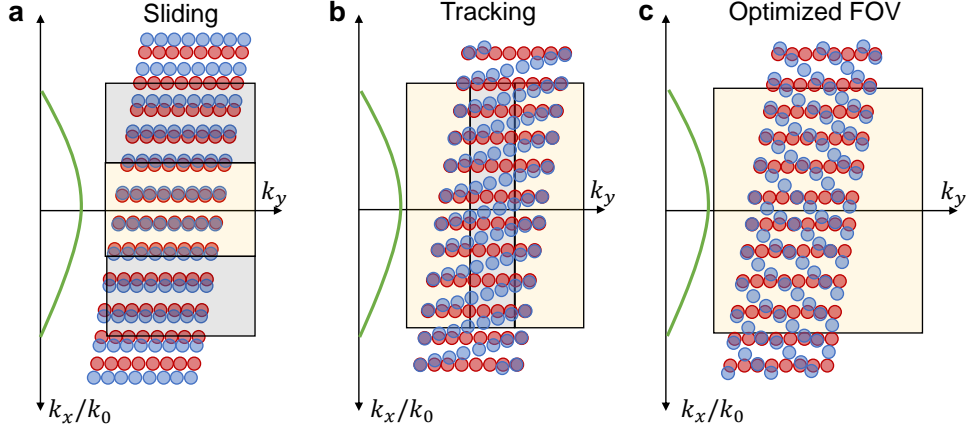
5

Fig. S3. Schematic depiction of achievable FOVs for different steering configuration and associated bandwidth usage. a Sliding steering configuration – the grating lobe-limited FOV is achieved and the wavelength bandwidth is used efficiently. The green line represents the element pattern FOV due to the individual grating widths, the maximum achievable FOV. The gold box denotes the set of angles and wavelengths which can be addressed by the Vernier transceiver. The gray boxes denote angles or wavelengths which are suppressed by the Vernier transceiver and cannot be addressed. **b** Tracking steering configuration – in theory the full $180°$ FOV is addressed by the aligned lobes, however the effective FOV is limited by the element pattern. The wavelengths at which the main lobes are outside this FOV (gray box) are not usable by the Vernier transceiver. **c** Controllable FOV steering configuration – the FOV is set to a desired width (here, the nulls of the element function) resulting in the entire bandwidth being utilized and an FOV larger than the grating lobe spacing.

transceiver, which is dependent on the steering configuration, and we denote this quantity as FOV_V.

One major problem for OPAs is the effect of fabrication errors. Pointing error, where the beam emission angle at the design wavelength is different than the desired angle, is one such effect. For OPAs using phase-shifter control, the pointing error is calibrated out at the same time as the emitter phases are corrected. For a single wavelength-steered OPA such as the SOPA, one can simply change the wavelength to correct this pointing error. However, for a pair of wavelength-steered OPAs used in a transceiver, this pointing error will result in misaligned TX and RX main lobes in addition to possible, unanticipated alignment of grating lobes.

The sliding mode (Fig. S3**a**, see also Supplementary Video 2) has the property of guaranteeing that two lobes will be aligned at some angle within the hemisphere due to the quality of the two lobes 'sliding' across each other within the FOV_V during a wavelength scan, and FOV_V remains limited to the grating lobe spacing FOV_G (see gray boxes in Fig. S3**a**, denoting in accessible angles). However, for misaligned TX and RX lobes arising from fabrication- or temperature-induced pointing error, this FOV_V may not be centered on broadside. The two most-aligned lobes are within this off-broadside FOV_V and, within a single fast scan, will become perfectly aligned at some angle due to the sliding property. This perfect alignment angle is the center angle of the FOV_V. For a $k = 1$ Vernier transceiver (see Eq. Eq. (S9)) an FOV_V scan will lead to a sliding of the transmitter spot fully over the receiver spot.

This contrasts with the tracking mode (Fig. S3**b**, see also Supplementary Video 3), where the relative alignment of every pair of lobes is locked in place throughout the wavelength scan. Notably the Vernier arrangement guarantees one pair of lobes to be nearly aligned. Additionally, because the alignment is locked in at all wavelengths, the limitations on FOV imposed by grating lobes are entirely removed. However, the element function FOV_E provides a limit on the angles which beams can be emitted to/received from, and FOV_V is simply FOV_E (centered on broadside). The tracking mode therefore addresses the issue of pointing error in wavelength-steered OPA transceivers in addition to expanding the FOV.

While tracking mode is clearly superior in this regard, there is a price paid for the increased FOV_V and guaranteed optimal alignment at some (possibly unknown) angle in wavelength-

steered OPAs like the SOPA. A significant portion of the full hemispherical lobe alignment of tracking mode is spent outside FOV_E (see gray box in Fig. S3**b**). This fact highlights that a portion of the wavelength scan is lost by scanning over angles where the OPA is incapable of transmitting or receiving a signal as the aligned lobes are directed outside the radiation pattern of a single grating. It is convenient at this point to consider that, for a given SOPA design with particular row-to-row delay, there is a set frequency shift required to move to the next resolvable spot along the fast axis. If the wavelength scan range is also set, then there is constant number of spots one can steer to. One can then see that the price of the guaranteed alignment and extended FOV_V of tracking mode is a reduction in the total number of usable, addressable spots. For sliding mode, when the perfect alignment angle is within the radiation pattern of a single grating, one can access all potential spots. The highest efficiency over the scan results when the alignment angle is in the middle (at the peak) of the single grating radiation pattern (element pattern in RF terminology), with bidirectional link efficiency decreasing towards the edges of the scan as the transmit and receive main lobes slide apart.

One additional difference between the two approaches should be noted, which is the set of spots that can be addressed. The use of 2D wavelength steering means that beam steering along both dimensions is not independent, any change in wavelength will steer the beam along both axes. The different scanning properties of tracking and sliding mode along the grating-orthogonal (x) direction then motivates design for different row-to-row phase accumulation rates. Ideally, the transceiver will steer to every spot within a 2D FOV_V without gaps. This requires that a fast scan across FOV_V steers the spot by one resolvable spot width *along* the grating dimension. Because the two steering modes have different FOV_V's, the different Vernier steering modes are optimized by different delay line lengths.

In order to benefit from the increased FOV_V of the tracking mode without 'missing' spots along the grating dimension, one needs to increase the row-to-row delay relative to the sliding mode (decreasing the frequency shift needed to steer by one spot along the grating-orthogonal dimension). For a TX OPA design with N grating lobes within the hemisphere, a design which meets this criterion would have $N\times$ larger row-to-row delay than the base design. This increases the number of spots within a full wavelength scan by a factor of N, while simultaneously decreasing the frequency to needed to steer to the next spot by a factor of $1/N$. Tracking mode therefore can address more spots than sliding mode because FOV_V is larger along the grating-orthogonal dimension while the spot size is unaffected. The price is the $N\times$ smaller frequency bandwidth available for operations such as ranging [6] and sub-spot imaging [7] which are bandwidth-limited to the frequency shift required to address the next resolvable spot. In addition, this $N\times$ larger delay will require a larger aperture, increase the effects of phase errors from fabrication non-uniformity, and reduce the bandwidth available for ranging and imaging.

6. STEERING CONFIGURATION FOR CONTROLLABLE FOV VERNIER

Considering these two steering options, it can be seen that although the sliding mode eliminates unwanted grating lobe returns, it still suffers from the conventional grating lobe-limited FOV_G and potential misalignment between TX and RX at the center of the FOV_V whereas tracking mode throws away some scan wavelengths which are outside the element function FOV_E. This suggests that a hybrid steering mode which exactly scans over the maximum possible angular range without throwing away any scan wavelengths. Here, the maximum FOV achievable is that limited by the radiation pattern of a single grating row width (the element pattern), FOV_E. This can be achieved by designing a Vernier which has lobes which slide apart on the order of lobe width over the desired $FOV_V \approx FOV_E$ (Fig. S3**c**, see also Supplementary Video 4), rather than sliding apart over FOV_G as in sliding mode. Tracking mode can be seen as the case where the lobes do not slide apart, so we require a delay relation between the TX/RX OPAs which is between the sliding and tracking delay relations.

We define the FOV_V for this controllable FOV Vernier in the same manner as the sliding mode: the angular range scanned over between perfect lobe alignment and the first peak-null lobe alignment. Considering the case of perfect lobe alignment at broadside, one needs simply to find the emitter phases which steers one lobe to one edge of FOV_V and the other lobe to the corresponding null.

For this situation, when the RX OPA main lobe is steered to the edge of FOV_V, the TX OPA main lobe is aligned with the RX null just outside the FOV in accordance with the null condition Eq. (S6) with $m = 1$. Denoting the angle corresponding to the edge of FOV_V as θ_{FOV}, the spatial frequency corresponding to the positive edge of FOV_V is

$$\beta_{\text{FOV}} = \frac{2\pi}{\lambda} \sin\left(\frac{\theta_{\text{FOV}}}{2}\right). \tag{S18}$$

Using this requirement, the relation in phase difference between the TX and RX OPAs for the hybrid steering configuration can be found as

$$\Delta\phi_{RX} = \frac{\Lambda_{RX}}{\Lambda_{TX}} \frac{1}{1 + \frac{2\pi}{\beta_{\text{FOV}}W}} \Delta\phi_{TX} \tag{S19}$$

where $W = W_{TX} = W_{RX}$ is the identical aperture width between the TX and RX OPAs enforced by the optimal lobe suppression condition.

The tracking and sliding configurations can be seen as limiting cases of this hybrid steering configuration. The tracking condition, in which the lobes never slide apart, therefore has an 'infinite' FOV (in the absence of an element function) and can be achieved by setting $\beta_{\text{FOV}} = \infty$ in Eq. (S19). The sliding condition, which has an FOV_V limited to the grating lobe spacing, can also be obtained from Eq. (S19) by setting $\beta_{\text{FOV}} = 2\pi/\Lambda_{RX}$.

7. PHASE ERRORS FOR BISTATIC APERTURES

The effects of phase errors are compounded by a bistatic aperture configuration, such as the Vernier approach, as compared to a monostatic aperture. As mentioned in the main text, phase errors within the OPA create a wider, non-ideal spot in comparison to the theoretical profile. To our knowledge these phase errors arise from layer thickness variation across the wafer, and within the OPA only changes in layer thickness contribute to phase errors (and not the average layer thickness). For wavelength-steered OPAs such as the SOPA, changes to average layer thickness only contribute to a 'pointing error', namely that the wavelength corresponding to emission at a certain angle will change with layer thickness. For a single OPA this is not an issue, one can simply adjust the wavelength tuning range, but for a pair of OPAs this could reduce or entirely negate the return signal if the pointing error is on the scale of, or greater than, the beam width. We conducted trial experiments with many pairs of SOPAs to find the optimal overlap and spot profile shown in this paper, with each pair separated by approximately 2 mm. Based on these trial experiments, this pointing error is non-negligible over the 6.4 cm path lengths used in our SOPA design, but negligible over the path length of an individual grating (0.8 mm). During the trial experiments, we noted that the spots of all pairs of SOPAs were effectively fully overlapping along the grating dimension, indicating negligible pointing errors over the grating path length. However, in many cases the spots were misaligned along the orthogonal (row-to-row) dimension to the extent that no significant return signal would be detectable. We did not characterize pointing error over larger OPA-to-OPA distances. It is possible to compensate for both intra- and inter-OPA phase errors using phase-shifters between rows, an approach we are pursuing in ongoing work, but those designs were not available for this experiment. The length scale over which the pointing error becomes relevant does indicate that the Vernier scheme, and bistatic aperture schemes in general, are well suited to 1D or 2D phase-shifter steered OPA designs due to their shorter path lengths in comparison to 2D wavelength-steered OPAs.

REFERENCES

1. T. Komljenovic, R. Helkey, L. Coldren, and J. E. Bowers, "Sparse aperiodic arrays for optical beam forming and lidar," Opt. express **25**, 2511–2528 (2017).
2. A. V. Oppenheim, *Discrete-time signal processing* (Pearson Education India, 1999).
3. F. J. Harris, "On the use of windows for harmonic analysis with the discrete fourier transform," Proc. IEEE **66**, 51–83 (1978).
4. K. O. Friedrichs, "The identity of weak and strong extensions of differential operators," Transactions Am. Math. Soc. **55**, 132–151 (1944).
5. L. C. Evans, *Partial differential equations*, vol. 19 (AMS Graduate Series in Mathematics, 2010).
6. N. Dostart, B. Zhang, A. Khilo, M. Brand, K. A. Qubaisi, D. Onural, D. Feldkhun, K. H. Wagner, and M. A. Popović, "Serpentine optical phased arrays for scalable integrated photonic lidar beam steering," Optica **7**, 726–733 (2020).
7. K. Wagner, D. Feldkhun, B. Zhang, N. Dostart, M. Brand, and M. Popović, "Super-resolved interferometric imaging with a self-cohering si-photonic beam-steering lidar array," in *Digital Holography and Three-Dimensional Imaging*, (Optical Society of America, 2019), pp. M5A–1.